

# Beam Corrections and Heterogeneous Arrays

## I: Total Intensity

W. D. Cotton (NRAO,SARAO), T. Mauch (SARAO) November 11, 2020

**Abstract**—We demonstrate a technique for correcting asymmetries in antenna patterns and differences among antennas using simulated data for a mixed array of 13.5 and 15 m antennas. This technique is tested in the Obit package and is shown to reduce the level of artifacts to near the level of those from the basic imaging technique. The flux densities and spectral indices of the sources in a realistic simulated sky model are well recovered. The additional computational expense is minor, 6% in the test described.

**Index Terms**—Antenna beam correction

### I. INTRODUCTION

ASYMMETRIES in alt-az mounted antennas introduce time dependent gain variations in the direction of sources off the axis as the antenna pattern rotates on the sky with parallactic angle. This is the equivalent of observing a time varying source and will introduce non-convolutional artifacts in the derived image. The use of heterogeneous arrays, arrays of antennas with dissimilar patterns on the sky, are an even more extreme case as the different antennas see a different effective sky even at the same time.

Antenna patterns in total intensity (Stokes I) are generally relatively symmetric whereas the corresponding patterns in off-axis instrumental polarization are generally not. An extended synthesis in polarization will tend to reduce these effects by averaging them out but at the cost of increased image noise. Widefield imaging in polarization may be seriously degraded by residual off-axis instrumental contributions.

If the antenna patterns on the sky are known, the effects on the derived image can be corrected in the deconvolution process. Previous attempts to correct antenna gain effects for a homogeneous array (EVLA) are described in [1] and [2]. This memo describes such a technique for total intensity and performs tests using simulations of the heterogeneous array MeerKAT+ (MeerKAT plus SKA dishes) as implemented in the Obit package [3]<sup>1</sup>.

### II. BEAM CORRECTIONS

There are two aspects of correcting images for the undesirable aspects of antenna patterns, 1) correcting total intensity images to remove the artifacts resulting from beam asymmetries and variations among antennas, and 2) removing the spurious polarized features introduced by the off-axis instrumental polarization response to total intensity.

The “A-projection” technique can correct for primary beam effects by the appropriate modification of the imaging gridding convolution kernel [4]. However, there are several complications from a simple application of this technique. If the response to the sky model is to be subtracted from the observed visibilities, the correction process must be reversed to “corrupt” the sky model derived from the corrected dirty image in the subtraction from the corrupted visibility data. The other complication is that correction of the dirty image for the primary beam amplifies the noise as a function of distance from the pointing center resulting in non-stationary noise. Corrections through a null in the antenna pattern will introduce extremely high noise in the corresponding regions of the image. Here we will consider corrections for total intensity based on a CLEAN deconvolution in which a corrected sky model is iteratively subtracted from the observed data. Consideration of polarization corrections is deferred to a subsequent study.

Corrections to the sky model visibilities are straightforward to add in a “DFT” model calculation technique in which the response to each sky model component is calculated explicitly for each visibility sample. This allows simple inclusion of temporally and spatially variant effects. The technique can be relatively expensive in terms of computing cycles but extremely efficient parallel CPU/vector and GPU implementations make the technique very competitive with FFT based calculations [5].

#### A. Total intensity

If the deviations of the antenna pattern from a “perfect” one is largely in amplitude, an image derived from the data without correction will produce emission in the proper location but with imperfect amplitude and with distortions and other artifacts. In each major CLEAN cycle, a shallow CLEAN in this case will select a sky model at locations where there is true emission and which contains some fraction of that emission. The transform of this sky model to the visibility domain can then make corrections for the undesirable aspects of the antenna pattern, basically multiplying by the actual antenna gains at the time of each visibility sample in the direction of each component of the sky model.

This has the undesirable side effect that it increases the uncertainty of the flux density of a given component in a radially dependent fashion. But, note that this does not affect the off-source noise in the image. To counter this effect, the correction to the sky model visibility is divided by the gain of a well behaved, symmetric beam pattern. This leaves the flux density of the model on approximately the same scale as the

National Radio Astronomy Observatory, 520 Edgemont Rd., Charlottesville, VA, 22903 USA email: bcotton@nrao.edu

South African Radio Astronomy Observatory, 2 Fir St., Observatory, South Africa

<sup>1</sup><http://www.cv.nrao.edu/~bcotton/Obit.html>

noise. The complex gain corrections are

$$g_{corr}(\nu, t, q, \alpha, \delta, a_1, a_2) = g_{a_1}(\nu, t, q, \alpha, \delta) g_{a_2}^*(\nu, t, q, \alpha, \delta) / g_{perfect}^2(\nu, \alpha, \delta)$$

where  $\nu$  is the frequency,  $t$  the time,  $q$  the polarization type,  $\alpha$  the right ascension,  $\delta$  the declination,  $a_1$ , the first antenna,  $a_2$  the second antenna,  $g^*$  indicates the complex conjugate and  $g_{perfect}^2$  is the power gain of a suitable, well behaved beam shape. For a sky model composed of  $n$  point components with flux density  $A_i$  and direction cosines  $l_i, m_i$  the calculated instrumental response is:

$$V_{model}(\nu) = \sum_{j=0}^n g_{corr}(\nu, t, q, \alpha, \delta, a_1, a_2) \times A_i(\nu) e^{-2\pi i(u_\nu l_j + v_\nu m_j + w_\nu n_j)}$$

where  $(u_\nu, v_\nu, w_\nu)$  is the uv plane coordinates and  $n_j = \sqrt{1 - l_j^2 - m_j^2}$ .  $V_{model}(\nu)$  is calculated for each visibility, subtracted from residual visibilities and a new dirty image is generated for the next major cycle. This subtracts the instrumental response to the sky model and after multiple major cycles, the image residuals will approach zero and the accumulated sky model will approach the actual sky brightness distribution as modified by the “perfect” beam.

### III. OBIT IMPLEMENTATION

The Obit classes `ObitSkyModelVMBeam` and `ObitSkyModelVMBeamMF` implement antenna beam corrections from one or more antenna types. These classes will calculate the instrumental response to a given sky model given a set of antenna beam gains. The antenna patterns are provided in the form of image cubes in the various visibility polarization products (RR,LL,RL,LR and XX,YY,XY and YX) and finely spaced in frequency. Lists of gains in the various products are interpolated at the position offsets of the CLEAN components for a given parallactic angle as described in Section II-A. As the parallactic angle changes, the gains are redetermined. Task `MFBeam` allows for the definition of the complex antenna patterns as a function of frequency and polarization for one or two antenna types. `MFBeam` (optionally) produces an output data file from which the sky model and any resultant instrumental polarization responses have been removed.

### IV. SIMULATIONS

The MeerKAT+ array will have 84 antennas located out to distances of nearly 10km from its center at latitude  $-30:42:39.8$ , longitude  $+21:26:38.0$ . The array will be made up of a ‘core’ consisting of the original MeerKAT 13.5 m dishes whose locations are shown as plus signs in Figure 1. These will be supplemented by a further 20 dishes primarily at greater distance from the array center, these will have a 15.0 m diameter SKA design (circles in Figure 1). The different apertures of the MeerKAT and SKA dishes result in them having significantly different attenuation patterns. Complex voltage patterns at 1510 MHz derived from simulations of the MeerKAT and SKA antenna optics made by the EMSS were provided by M. De Villiers and are shown in Figure 2.

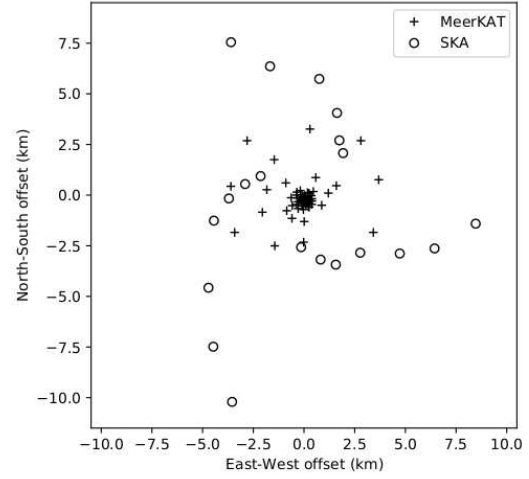


Fig. 1. The MeerKAT+ array configuration used in the simulation. Positions of antennas are shown in km relative to the array center at latitude  $-30:42:39.8$ , longitude  $+21:26:38.0$ . The positions of the 64 13.5 m diameter MeerKAT dishes are shown as plus signs and the 20 15.0 m SKA dishes are shown as circles.

#### A. Simulation framework

A framework that mimics a `katdal`<sup>2</sup> dataset was used for generation of visibilities and metadata from a simulated MeerKAT+ array. A simulated `katdal` dataset is useful since future MeerKAT+ pipelines will use this format for their input, thus allowing for easy integration of imaging routines into candidate MeerKAT+ pipelines. Also, methods currently in use for MeerKAT that convert visibilities and metadata from `katdal` datasets into AIPS UV format used by `MFBeam` and `MFIimage` can be reused. A simulated MeerKAT+ observation using this framework requires the following inputs:

- The right ascension ( $\alpha$ ) and declination ( $\delta$ ) of a pointing center (multiple pointing centers can be defined). Also a list of activities defining the state of the telescope, the length of time in the given state (defined in number of time steps) and the telescope pointing center while in each state.
- A list of spectral windows, defining the frequency setup of the simulated observation (i.e. number of channels, center frequency and channel width).
- A dictionary of subarrays defining the antenna configuration to be used in the simulation. Antenna positions are defined with `katpoint`<sup>3</sup> using their ENU coordinates relative to a WGS84 array center (Lat.:  $-30:42:39.8$ , Long.:  $+21:26:38.0$ , Altitude: 1086.6 m for MeerKAT+).
- A dictionary describing the start time (seconds from UNIX epoch) and the dump period (seconds) of the observation.
- Three functions that compute visibilities, weights and flags for the observation, these return 3d arrays of shape (number of timesteps, number of channels, number of correlation products). For the MeerKAT+ simulations described in this memo the weights are all set to 1.0 and

<sup>2</sup><https://github.com/ska-sa/katdal>

<sup>3</sup><https://github.com/ska-sa/katpoint>

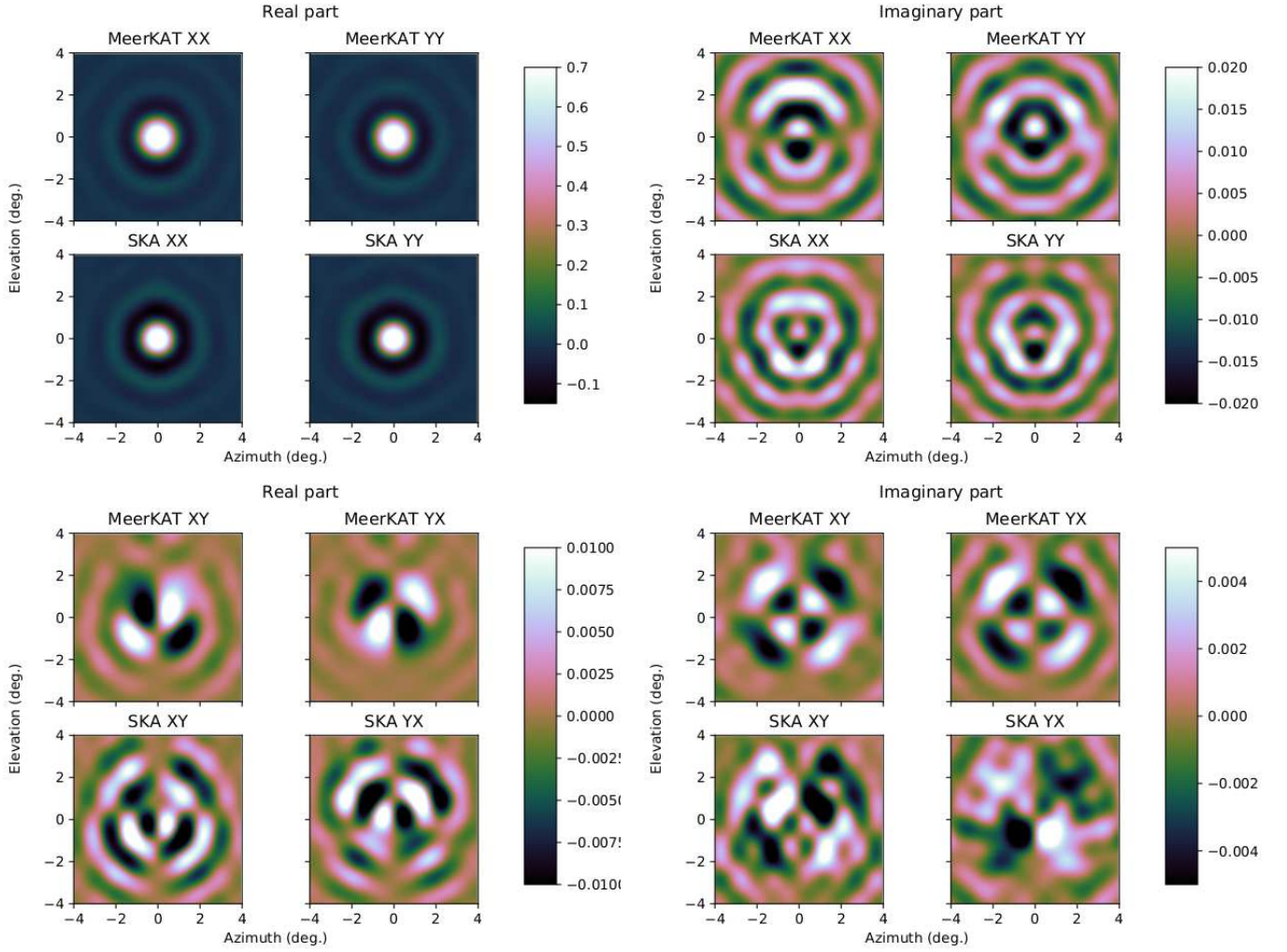


Fig. 2. Real (left) and imaginary (right) parts of the complex voltage patterns at 1510 MHz used in the simulation for 13.5 m MeerKAT dishes and 15.0 m SKA dishes (as labelled). The co-polarization response is shown in the top two rows and the cross-polarization in the bottom two.

no flags are defined. A function describing the returned visibilities is described in Section IV-B.

- A dictionary of metadata describing the observation (names, descriptions etc.)

The simulations described in this memo all use a pointing center at  $\alpha = 0^h$ ,  $\delta = -80^\circ$ , with a single ‘track’ of 120 time samples over a 12 hour observation period starting at 1970-01-01T15:50:15 UTC (when the array pointing has parallactic angle  $q \sim 0^\circ$ ). The MeerKAT+ frequency range at L-band was sampled with 64 channels over the range 898.8–1669.2 MHz and the 84 antennas with positions and types as shown in Figure 1.

### B. Simulated visibilities

The simulation defines a function that computes complex visibilities given the observational setup described in Section IV-A and a list of point sources to be simulated. The visibilities are simulated using the Müller and Jones matrix formalism described by [6] and references therein.

The flux density of any point source at a given right ascension ( $\alpha$ ) and declination ( $\delta$ ) is specified with a model

describing the intrinsic Stokes  $I(\nu), Q(\nu), U(\nu), V(\nu)$  flux densities of the source as a function of frequency  $\nu$ . These flux densities are then converted to linearly polarized coherencies at each channel frequency using:

$$\begin{bmatrix} B_{XX} \\ B_{XY} \\ B_{YX} \\ B_{YY} \end{bmatrix} = \begin{bmatrix} 1 & 1 & 0 & 0 \\ 0 & 0 & 1 & j \\ 0 & 0 & 1 & -j \\ 1 & -1 & 0 & 0 \end{bmatrix} \begin{bmatrix} I \\ Q \\ U \\ V \end{bmatrix}, \quad (1)$$

this is Equation 4.55 of [7]. These intrinsic receptor coherencies are then formed into the  $2 \times 2$  Jones matrix

$$B(\nu) = \begin{bmatrix} B_{XX} & B_{XY} \\ B_{YX} & B_{YY} \end{bmatrix} \quad (2)$$

which is computed for each simulated channel with frequency  $\nu$ ; the flux densities of simulated sources are assumed to be constant over time.

The antenna voltage responses of each linear polarisation shown in Figure 2 will scale the intrinsic coherencies  $B(\nu)$  of a point source differently for each timestamp and baseline. For an antenna  $a$ , the value of the voltage response at the position of the source at  $(\alpha, \delta)$  with direction cosine coordinates  $(l, m)$

relative to the phase centre is scaled and rotated to coordinates  $(l'_a, m'_a)$ . The coordinates  $(l'_a, m'_a)$  are derived from

$$\begin{bmatrix} l'_a(t, \nu) \\ m'_a(t, \nu) \end{bmatrix} = \left( \frac{\nu}{\nu_{\text{ref}}} \right) \begin{bmatrix} \cos q_a(t) & \sin q_a(t) \\ -\sin q_a(t) & \cos q_a(t) \end{bmatrix} \begin{bmatrix} l \\ m \end{bmatrix}, \quad (3)$$

where the fraction  $\frac{\nu}{\nu_{\text{ref}}}$  radially scales the  $(l, m)$  coordinates from the reference frequency ( $\nu_{\text{ref}}$ ) of the beam images in Figure 2 (1510 MHz) to the frequency of interest and the source position is rotated (in an *anti*-clockwise direction) by the parallactic angle  $q_a(t)$  of the antenna  $a$  at time  $t$ .

The complex-valued beam voltages  $E_{XX}(l'_a, m'_a)$ ,  $E_{XY}(l'_a, m'_a)$ ,  $E_{YX}(l'_a, m'_a)$  and  $E_{YY}(l'_a, m'_a)$  for an antenna are obtained from a bi-cubic interpolation of the beam voltage patterns in Figure 2. These are then formed into the  $2 \times 2$  Jones matrix

$$E_a(t, \nu, l, m) = \begin{bmatrix} E_{XX}(l'_a, m'_a) & E_{XY}(l'_a, m'_a) \\ E_{YX}(l'_a, m'_a) & E_{YY}(l'_a, m'_a) \end{bmatrix}, \quad (4)$$

for each simulated timestamp ( $t$ ), frequency ( $\nu$ ) and antenna ( $a$ ). The Jones matrix describing the beam-scaled flux density  $F$  for a baseline between two antennas  $a_1$  and  $a_2$  is then

$$F(t, \nu, l, m, a_1, a_2) = E_{a_1}(t, \nu, l, m) \times B(\nu) \times E_{a_2}^\dagger(t, \nu, l, m) \quad (5)$$

where the term  $E_{a_2}^\dagger$  represents the complex conjugate and transpose of the matrix  $E_{a_2}$ . The flux density matrix  $F$  describes the variation in the measured coherencies caused by differences in per-antenna voltage patterns in heterogeneous arrays (i.e.  $F$  is a function of *baseline*, and if the antenna type of  $a_1$  is MeerKAT and  $a_2$  is SKA then  $E_{a_1} \neq E_{a_2}$ ). It further includes the effect of variations due to beam asymmetries (i.e.  $F$  is a function of *time*, and  $E_{XX}(l', m')$  etc. will vary as a source position rotates with parallactic angle in a non-symmetric voltage pattern).

A  $2 \times 2$  Jones matrix of a simulated visibility for a single point source  $i$ , is

$$V_i(t, \nu, l_i, m_i, a_1, a_2) = F_i(t, \nu, l_i, m_i, a_1, a_2) \times e^{-2\pi j(u_\nu l_i + v_\nu m_i + w_\nu(n_i - 1))}, \quad (6)$$

at a position given by direction cosines  $(l_i, m_i, n_i = \sqrt{1 - l_i^2 - m_i^2})$ , on a baseline between antennas  $a_1, a_2$  with UV-plane coordinates  $(u_\nu, v_\nu, w_\nu)$  (measured in wavelengths at the given frequency). When simulating  $N$  point sources in the field the visibility for a given baseline, frequency and timestamp is

$$V(t, \nu, a_1, a_2) = \sum_{i=1}^N \frac{V_i(t, \nu, l_i, m_i, a_1, a_2)}{n_i}. \quad (7)$$

In practice, when producing a complex-valued array that is returned by a function that simulates the visibilities, the  $2 \times 2$  matrix  $V$  is unravelled into its 4 constituent polarizations for each timestamp, channel and baseline, and these are concatenated and sorted as required into a visibility array with 3 dimensional shape: number of times, number of channels and  $4 \times$  number of baselines.

## V. SIMULATION TESTS

Simulated data sets were imaged in Obit Task MFBeam which was given complex beam models for the MeerKAT and SKA antennas in all four Stokes correlations (XX, YY, XY, YX) on a fine grid of frequencies. MFBeam uses faceting to correct for the “w” term and multiple frequency bins are imaged independently but CLEANed jointly to accomodate the spatially variant sky spectral distributions and antenna gain patterns. Since the locations of sources are generally in a random location in a facet and the dynamic range desired is high, the Obit autoCenter feature is used in which sources with peaks in excess of 10 mJy/bm are imaged centered in their own facets and “unboxes” are placed around the corresponding locations of other facets. The depth of any major cycle is restricted to no deeper than 75% of the initial peak residual flux density. For comparison, the data were also imaged in the same way by MFImage in which beam corrections are not made.

Imaging was done on a Linux workstation running RHEL 7 with 16 x Intel(R) Xeon(R) CPU E5-2687W 0 @ 3.10GHz cores and 256 GByte of RAM, of which 100 GByte was configured into a RAM disk which was used for output and scratch files. This machine supports AVX but does not have a GPU.

### A. Source Grid

The first simulation was of a grid of  $3 \times 3$  0.1 Jy point sources separated by  $20'$  with no noise. The simulation was of the MeerKAT+ array consisting of MeerKAT (diameter 13.5m) plus 20 outlying antennas of the SKA design (15m) as described in Section IV. The beam models for tests were frequency cubes derived from the beam images shown in Figure 2 by a frequency scaling. All image models contained only Stokes I emission. The CLEAN was restricted to a radius of 5 pixels around the source position and CLEANing proceeded to 10,000 components. The data were imaged in both MFImage, which applied no antenna gain corrections, and MFBeam which does. Both tasks used the same imaging parameters.

Cutouts around the sources imaged by MFImage are shown in Figure 3 and from MFBeam in Figure 4 with a much smaller range of values displayed. The general level of artifact in Figure 4 is greatly reduced from Figure 3 although with some residual artifacts. The RMS residual in the imaging without beam corrections was  $1.3 \mu\text{Jy/bm}$  and with correction was  $0.076 \mu\text{Jy/bm}$ , a factor of 17 less.

The simulation was repeated except using the same, symmetric beam shape for all antennas. Imaging of this data with MFImage should not be affected by residual beam artifacts and show only the residual artifacts from imaging. Such results are shown in Figure 5 and should be compared with Figure 4. The bulk of the residual artifacts in Figure 4 appear not to be the result of uncorrected beam effects. The RMS residual was  $0.053 \mu\text{Jy/bm}$  or 40% less than for Figure 4.

### B. SKADS

The Square Kilometer Array Design Study (SKADS) developed a suite of simulations of the radio sky referred to

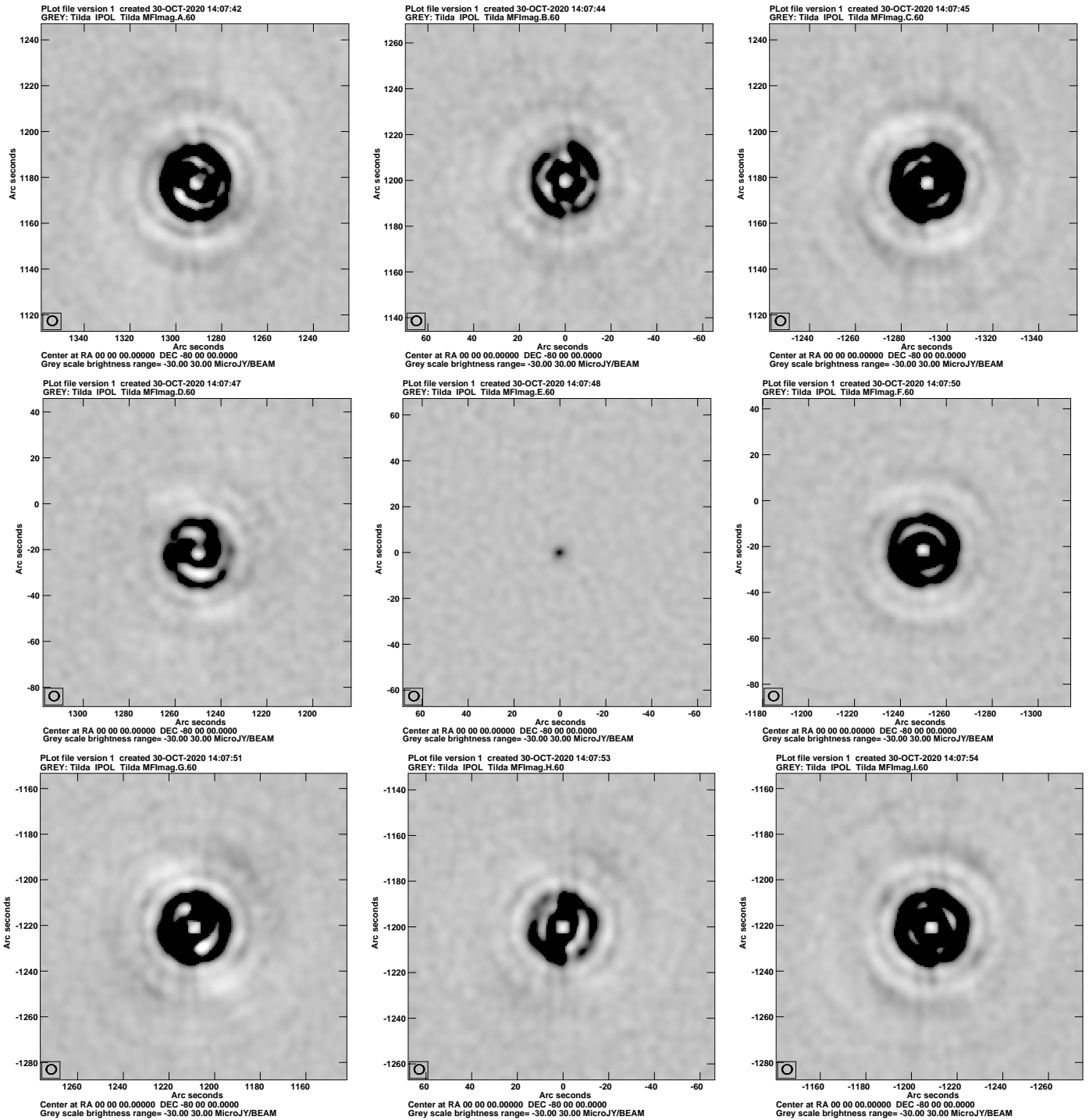


Fig. 3. Reverse gray scale of the CLEAN residuals in regions around the 9 simulated sources imaged without taking beam shapes into account. CLEANING was autoCentered with a CLEAN window of radius 5 pixels. The pixel range displayed is  $-30 \mu\text{Jy}$  to  $+30 \mu\text{Jy}$ . RMS noise is  $1.3 \mu\text{Jy/bm}$ . The resolution is shown in the box in the lower left.

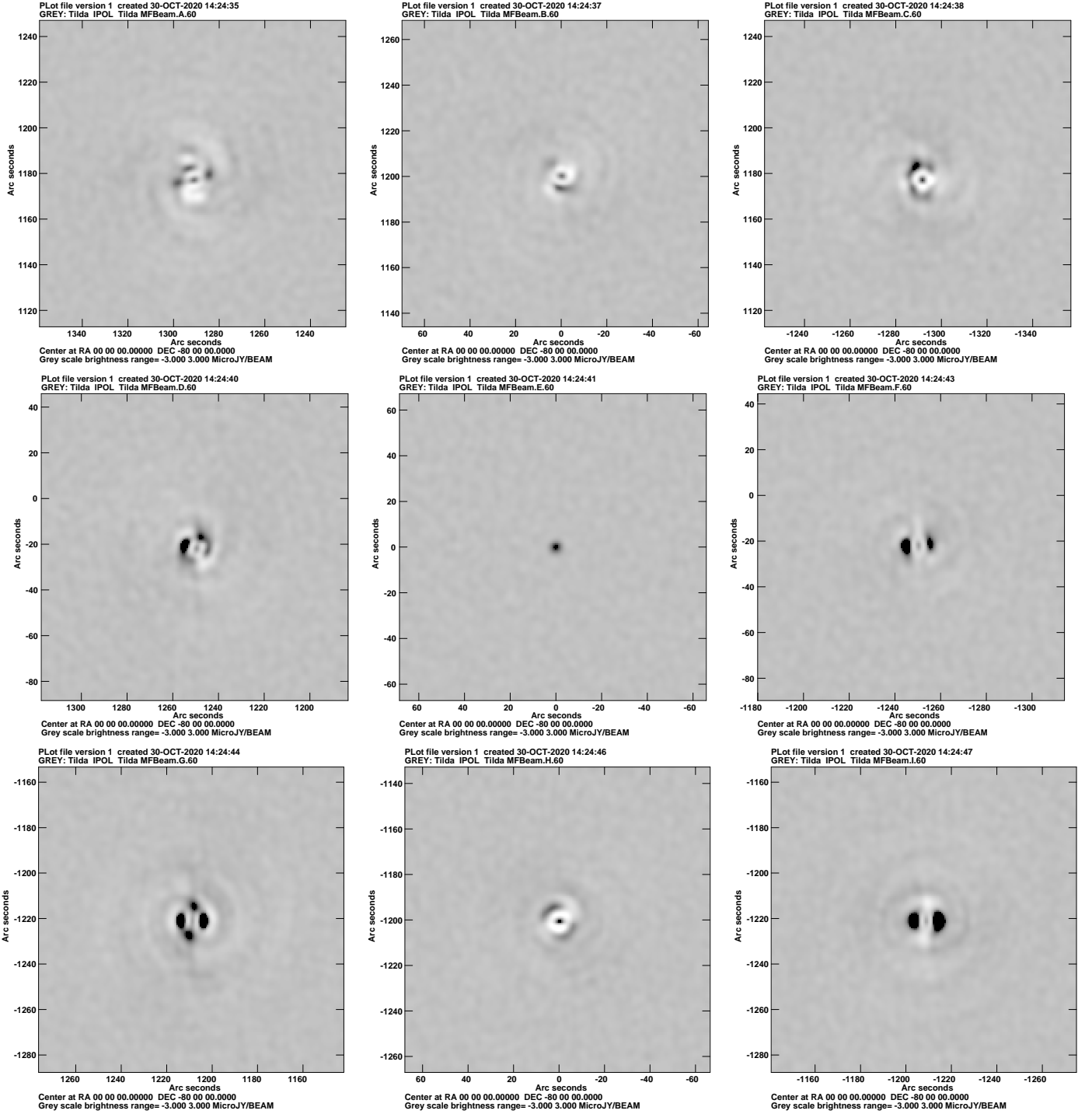


Fig. 4. Reverse gray scale of the CLEAN residuals in regions around the 9 simulated sources imaged taking beam shapes into account. CLEANING was autoCentered with a CLEAN window of radius 5 pixels. The pixel range displayed is  $-3 \mu\text{Jy/bm}$  to  $+3 \mu\text{Jy/bm}$ , this is 10% of the range displayed in Figure 3. RMS noise is  $0.076 \mu\text{Jy/bm}$ . The resolution is shown in the box in the lower left.

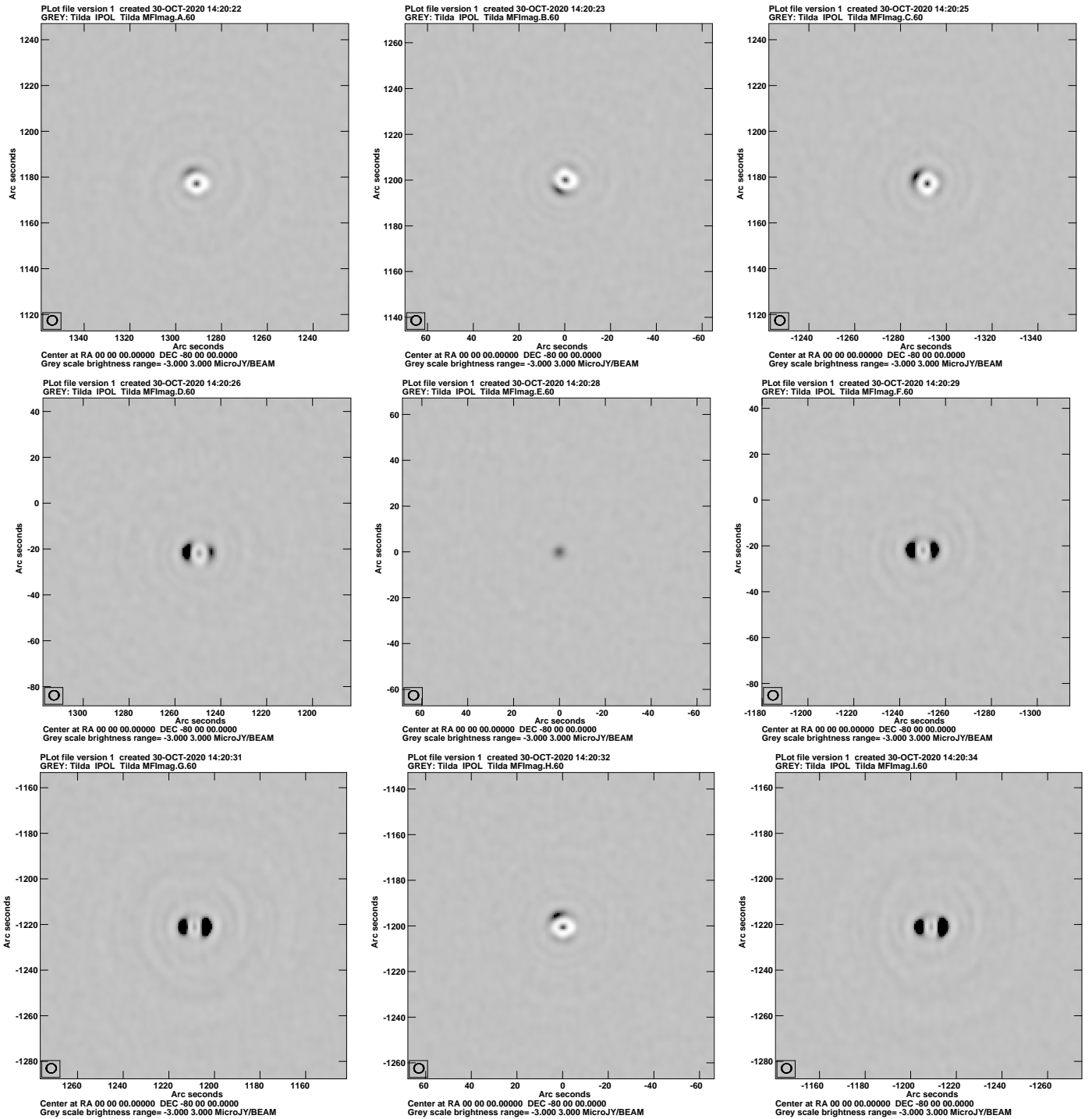


Fig. 5. Reverse gray scale of the CLEAN residuals in regions around the 9 simulated sources using a symmetric beam and CLEANed with MFIImag. To be compared with Figure 4. CLEANing was autoCentered with a CLEAN window of radius 5 pixels. The pixel range displayed is  $-3 \mu\text{Jy/bm}$  to  $+3 \mu\text{Jy/bm}$ . RMS noise is  $0.053 \mu\text{Jy/bm}$ . The resolution is shown in the box in the lower left.

collectively as the *SKADS Simulated Skies* ( $S^3$ ). The  $S^3$  Semi-Empirical eXtragalactic ( $S^3$ -SEX; [8]) simulation was constructed by drawing radio sources at random from observed and extrapolated radio luminosity functions for various radio source populations and positioning them with regard to a realistic model of their spatial clustering. The  $S^3$ -SEX *galaxies* simulation catalogue contains positions in a sky area of  $20^\circ \times 20^\circ$  and Stokes I flux densities derived from a model of the frequency dependence for each galaxy population at 5 frequencies between 0.151 and 18 GHz to a limit of 10 nJy. A region containing 2401 galaxies within a  $1^\circ$  radius to a 1400 MHz flux density limit of  $100 \mu\text{Jy}$  was used to provide a realistic input sky model for generating noiseless visibilities with the heterogeneous MeerKAT+ configuration. Each of the simulated point sources was fitted with a spectrum including a spectral index and up to 2 curvature terms. Beam images and source polarizations were as described in Section V-A.

This realistic sky simulation was imaged with and without beam corrections. Imaging consisted of a CLEAN of 100,000 components reaching a depth of  $\sim 10 \mu\text{Jy}/\text{beam}$ . The loop gain was 0.1 and each major cycle was limited to CLEANing to a depth of 0.75 times the initial maximum residual. The beam corrections resulted in the effective beam being the MeerKAT, nominal, symmetric pattern.

Imaging with MFImage (no corrections) took 5.05 hours of real and 25.7 hours of CPU time; MFBeam (with corrections) took 5.37 hours of real and 32.9 hours of CPU time, or 6% longer wall clock time. Of the increased run time of MFBeam, about half was in the extra subtraction of the total sky model from the input data.

Without beam corrections, the off-source RMS was  $2.60 \mu\text{Jy}/\text{bm}$  and with beam corrections  $0.55 \mu\text{Jy}/\text{bm}$ . The peak in the image is 0.55 Jy so the nominal dynamic ranges were  $1.0 \times 10^6$  with beam correction and  $2.1 \times 10^5$  without. Cutouts around some of the stronger sources imaged by MFImage (no beam correction) are shown in Figure 6 and the same sources imaged by MFBeam (beam corrected) in Figure 7 with the same stretch. The beam corrections greatly reduced the artifacts.

This simulation was also repeated except using the same, symmetric beam shape for all antennas. Imaging of this data with MFImage should show only the residual artifacts from imaging. Such results are shown in Figure 8 and should be compared with Figure 7. The bulk of the residual artifacts in Figure 7 appear not to be the result of uncorrected beam effects.

A comparison of the recovered flux densities (Obit/FndSou) after a correction for the primary beam attenuation is shown in Figure 9. This figure shows that the flux densities in the input model are well recovered, although a (CLEAN?) bias appears to be present in the outer parts of the image where the signal-to-noise ratio is lower and the beam gain is low.

The input model consisted of point sources with a variety of spectra. The derived image had spectra fitted in each pixel with flux density at the reference frequency and spectral index and up to 2 curvature terms. The fitted spectral indices after correction for the primary beam gain are compared with the input model values in Figure 10. The bulk of the fitted values

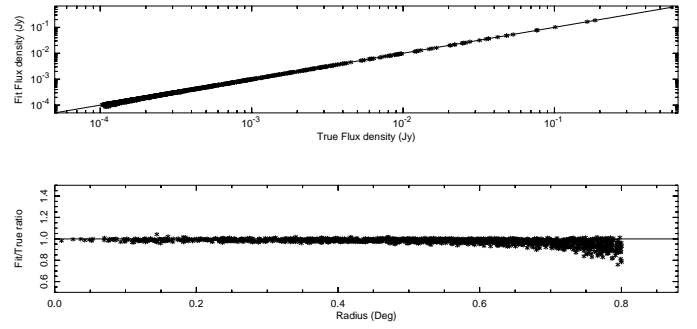


Fig. 9. Comparison of recovered ('Fit') source flux densities to true values. Top panel, the log "fitted" v. the log true values. The line shows the 1:1 values. The bottom panel gives the ratio of fit to true flux densities as a function of the distance from the pointing center.

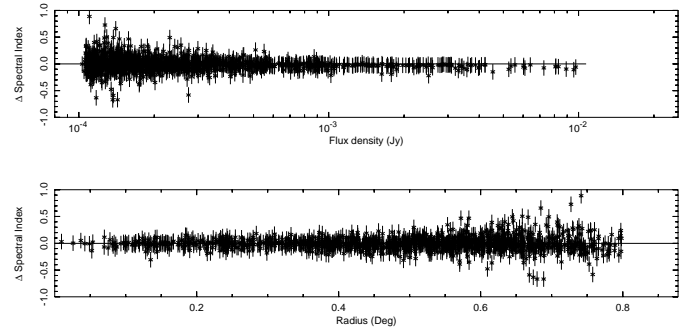


Fig. 10. Difference between the fitted and true spectral index as a function of flux density and distance from the pointing center with fitting error bars. Top panel, the fitted spectral index difference v. log flux density. The line shows the expected value (0.0). The bottom panel gives the spectral index difference as a function of the distance from the pointing center.

are close to the input model values but with some scatter which increases for weaker sources and increasing distance from the pointing center.

## VI. DISCUSSION

A technique for correcting for the beam shapes in a heterogeneous array is described and tested using simulated data. The basic technique is to ignore beam differences and asymmetries in making the dirty/residual images and then using a detailed model of the instrumental response in subtracting the model in each CLEAN major cycle. The simulated array, MeerKAT+, is a combination of 13.5 and 15 m antennas with model, asymmetric beam shapes. Both a test with a sparse grid of strong sources and a realistic sky simulation show a very significant improvement in the level of residual artifacts and off-source noise. The images after beam corrections had residual artifacts comparable to those in a simulation in which all antennas used the same, symmetric beam. In the realistic sky test, including the beam corrections increased the wall clock run time by 6%. The flux densities and spectral indices of the sources in the realistic sky model were well recovered from the image produced (Figures 9, 10).

## REFERENCES

- [1] W. D. Cotton and R. Perley, "EVLA Off-axis Beam and Instrumental Polarization," *Obit Development Memo*



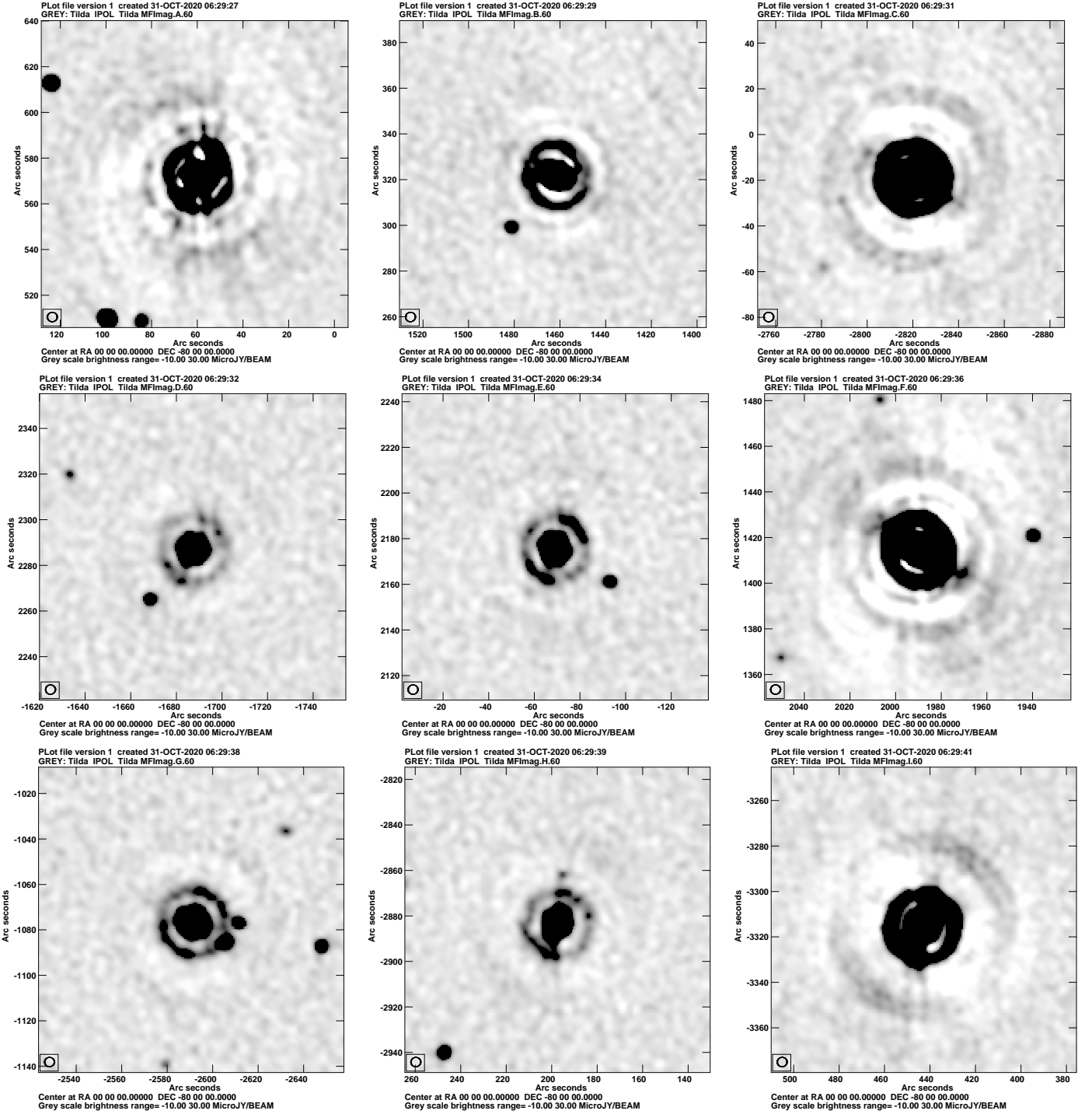


Fig. 6. Reverse gray scale of the CLEAN restored image in regions around 9 brighter sources in the SKADS simulation without taking beam shapes into account. CLEANing was autoCentered with auto windowing. The pixel range displayed is  $-10 \mu\text{Jy}$  to  $+30 \mu\text{Jy}$ . Off-source RMS noise is  $2.60 \mu\text{Jy/bm}$ . The resolution is shown in the box in the lower left.

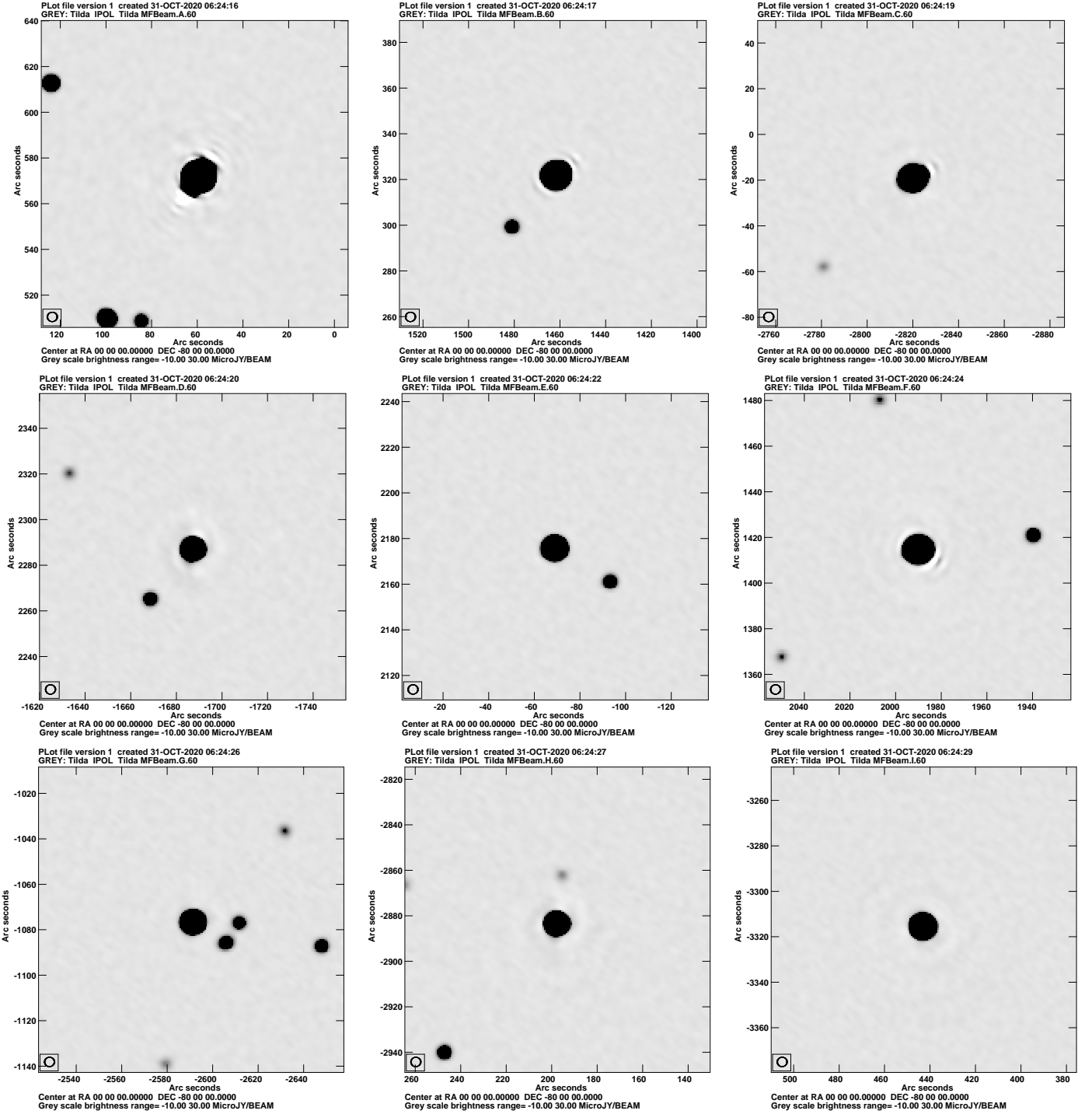


Fig. 7. Reverse gray scale of the CLEAN restored image in regions around 9 brighter sources in the SKADS simulation as in Figure 6 but taking beam shapes into account. CLEANing was autoCentered with auto windowing. The pixel range displayed is  $-10 \mu\text{Jy/bm}$  to  $+30 \mu\text{Jy/bm}$ . Off-source RMS noise is  $0.55 \mu\text{Jy/bm}$ . The resolution is shown in the box in the lower left.

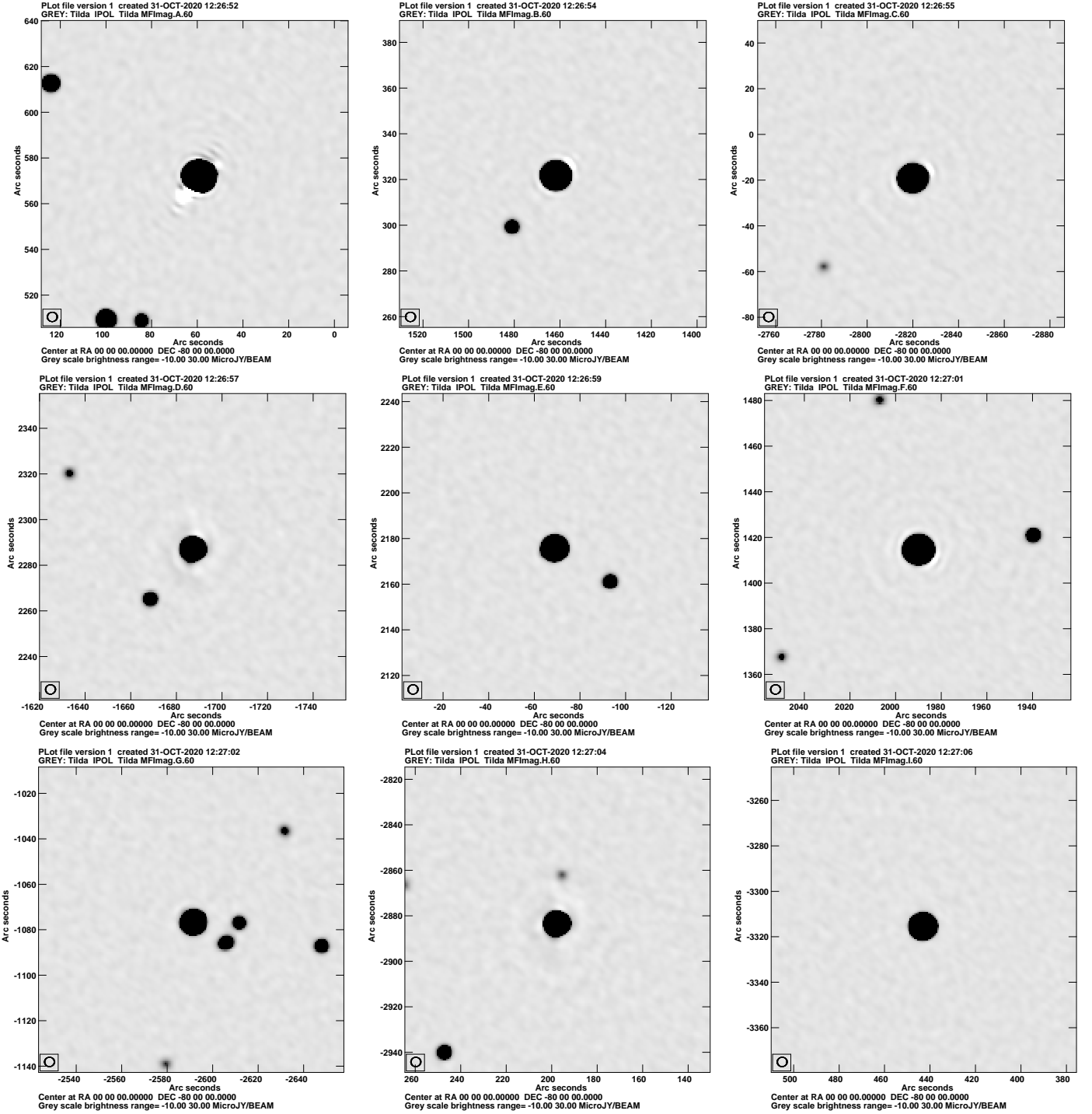


Fig. 8. Reverse gray scale of the CLEAN restored image in regions around 9 brighter sources in the SKADS simulation as in Figure 6 but with data simulated using a common, symmetric beam pattern. CLEANing was autoCentered with auto windowing. The pixel range displayed is  $-10 \mu\text{Jy/bm}$  to  $+30 \mu\text{Jy/bm}$ . Off-source RMS noise is  $0.84 \mu\text{Jy/bm}$ . The resolution is shown in the box in the lower left.

- Series*, vol. 17, pp. 1–22, 2010. [Online]. Available: <ftp://ftp.cv.nrao.edu/NRAO-staff/bcotton/Obit/EVLABeam.pdf>
- [2] —, “EVLA Beam Holography take 2,” *Obit Development Memo Series*, vol. 47, pp. 1–13, 2017. [Online]. Available: <ftp://ftp.cv.nrao.edu/NRAO-staff/bcotton/Obit/EVLABeam17.pdf>
- [3] W. D. Cotton, “Obit: A Development Environment for Astronomical Algorithms,” *PASP*, vol. 120, pp. 439–448, 2008.
- [4] S. Bhatnagar, T. J. Cornwell, K. Golap, and J. M. Uson, “Correcting direction-dependent gains in the deconvolution of radio interferometric images,” *A&A*, vol. 487, p. 419, 2008.
- [5] W. D. Cotton, “Comparison of GPU and Multithreading for Interferometric DFT Model Calculation,” *Obit Development Memo Series*, vol. 35, pp. 1–5, 2014. [Online]. Available: <ftp://ftp.cv.nrao.edu/NRAO-staff/bcotton/Obit/GPUDFTv2.pdf>
- [6] O. M. Smirnov, “Revisiting the radio interferometer measurement equation. I. A full-sky Jones formalism,” *A&A*, vol. 527, p. A106, Mar. 2011.
- [7] A. R. Thompson, J. M. Moran, and J. Swenson, George W., *Interferometry and Synthesis in Radio Astronomy, 3rd Edition*. Springer, 2017.
- [8] R. J. Wilman, L. Miller, M. J. Jarvis, T. Mauch, F. Levrier, F. B. Abdalla, S. Rawlings, H. R. Klöckner, D. Obreschkow, D. Olteanu, and S. Young, “A semi-empirical simulation of the extragalactic radio continuum sky for next generation radio telescopes,” *MNRAS*, vol. 388, no. 3, pp. 1335–1348, Aug. 2008.